A&A, 683, A138 (2024)
https://doi.org/10.1051/0004-6361/202347188

Astronomy
&
Astrophysics

Production of *s*-process elements in asymptotic giant branch stars as revealed by *Gaia*/GSP-Spec abundances

G. Contursi[1], P. de Laverny[1], A. Recio-Blanco[1], P. A. Palicio[1], and C. Abia[2]

[1] Université Côte d'Azur, Observatoire de la Côte d'Azur, CNRS, Laboratoire Lagrange, Bd de l'Observatoire, CS 34229, 06304 Nice Cedex 4, France
e-mail: `gabriele.contursi@oca.eu`
[2] Departmento de Fısica Teórica y del Cosmos, Universidad de Granada, 18071 Granada, Spain

Received 14 June 2023 / Accepted 16 September 2023

ABSTRACT

Context. The recent parameterisation by the GSP-Spec module of *Gaia*/Radial Velocity Spectrometer stellar spectra has produced an homogeneous catalogue of about 174 000 asymptotic giant branch (AGB) stars. Among the 13 chemical elements presented in this *Gaia* third data release, the abundance of two of them (cerium and neodymium) have been estimated in most of these AGB stars. These two species are formed by slow neutron captures (*s*-process) in the interior of low- and intermediate-mass stars. They belong to the family of second-peak *s*-process elements.

Aims. We study the content and production rate of Ce and Nd in AGB stars, using the atmospheric parameters and chemical abundances derived by the GSP-Spec module.

Methods. We defined a working sample of 19 544 AGB stars with high-quality Ce and/or Nd abundances, selected by applying a specific combination of the GSP-Spec quality flags. We compared these abundances with the yield production predicted by AGB evolutionary models.

Results. We first confirmed that the majority of the working sample is composed of AGB stars by estimating their absolute magnitude in the *K*-band and their properties in a *Gaia*-2MASS diagram. We also checked that these stars are oxygen-rich AGB stars, as assumed during the GSP-Spec parameterisation. We found a good correlation between the Ce and Nd abundances, confirming the high quality of the derived abundances and that these species indeed belong to the same *s*-process family. We also found higher Ce and Nd abundances for more evolved AGB stars of similar metallicity, illustrating the successive mixing episodes enriching the AGB star surface in *s*-process elements formed deeper in their stellar interior. We then compared the observed Ce and Nd abundances with the FRUITY and Monash AGB yields and found that the higher Ce and Nd abundances cannot be explained by AGB stars of masses higher than 5 $M_{\odot}$. In contrast, the yields predicted by both models for AGB stars with an initial mass between ~1.5 and ~2.5 $M_{\odot}$ and metallicities between ~−0.5 and ~0.0 dex are fully compatible with the observed GSP-Spec abundances.

Conclusions. This work based on the largest catalogue of high-quality second-peak *s*-element abundances in oxygen-rich AGB stars allows evolutionary models to be constrained and confirms the fundamental role played by low- and intermediate-mass stars in the enrichment of the Universe in these chemical species.

Key words. Galaxy: abundances – Galaxy: disk – stars: evolution – stars: abundances – stars: AGB and post-AGB

1. Introduction

Asymptotic giant branch (AGB) stars correspond to the late evolutionary stages of low-mass (masses smaller than ~3 $M_{\odot}$) and intermediate-mass (between ~4 and ~8 $M_{\odot}$) stars. Due to their specific internal structure, efficient mixing events, and high mass-loss rates, AGB stars are among the main contributors to the interstellar medium enrichment in several species. They hence play a fundamental role in the chemical evolution of the Universe (Ulrich 1973). Among all the elements produced by AGB stars, there are neutron-capture elements formed through the slow neutron-capture process (so-called *s*-process) that are of special interest. Indeed, Solar System abundance distribution of elements formed through the *s*-process show three peaks located around the atomic mass numbers $A = 90$, 138, and 208 (corresponding to the magic number of neutrons: 50, 82, and 126). While massive stars ($\gtrsim$8−10 $M_{\odot}$) and massive AGB stars are the main contributors of first-peak *s*-elements (Peters 1968; Lamb et al. 1977; Pignatari et al. 2010; Limongi & Chieffi 2018), species of the second peak, such as Ce and Nd, are mainly formed within AGB stars of lower masses, in which the main neutron source is the ^{13}C(α,n)^{16}O reaction (Arlandini et al. 1999; Busso et al. 1999; Karakas & Lattanzio 2014; Bisterzo et al. 2011, 2015). Finally, third-peak *s*-process elements, such as Pb, are thought to be predominantly formed within low-mass and low-metallicity AGB stars (Gallino et al. 1998; Choplin et al. 2022).

We emphasise that the internal structure of an AGB star (mass ≤8 $M_{\odot}$) is comprised by a compact and degenerated C−O core, a thin He-burning shell, and an H-burning shell separated by an He-intershell (composed of about 75% of He and 22% of C according to Karakas et al. 2002). All of these components are surrounded by a convective H- (and He-) rich envelope that is plagued by large mass-loss rates (from 10^{-8} to 10^{-4} $M_{\odot}$ yr^{-1}). During the AGB phase, material formed in the internal layers of the star (such as carbon and *s*-process elements) is brought to the surface by successive penetration of the convective envelope in the He-intershell. This phenomenon is known as the third dredge-up, or TDU (see, e.g., Straniero et al. 2003). During their lifetime, AGB stars experience several thermal pulses

(TPs) and hence several mixing episodes (referred as several TDU episodes, hereafter). However, the number of TPs strongly depends on the mass loss as well as on the initial mass and metallicity, and the TPs affect the nucleosynthesis occurring within AGB stars. Actually, theoretical predictions of the number of TPs for a given star are still rather uncertain since the lifetime of AGB stars is not well known.

Several stellar evolution models including nucleosynthesis of *s*-process elements have been developed to interpret the observed chemo-physical properties of AGB stars. The two most complete AGB models published up to now are the FRUITY (Cristallo et al. 2009, 2011, 2015) and the Monash models (Lugaro et al. 2012; Fishlock et al. 2014; Karakas & Lugaro 2016; Karakas et al. 2018). Both sets of models have their own AGB nucleosynthesis prediction that may differ due to the different physical assumptions adopted during each model's computation. The predicted yields are essential for the computation of chemical evolution models but also for direct comparison with the observed chemical composition of AGB stars. However, we note that because of the rather large number of free parameters, AGB models are adjusted to match observations (Lugaro et al. 2016). Therefore, a precise comparison between observed and predicted abundances is still mandatory in order to validate the different assumptions adopted in these complex models.

On the observational side, few studies have been devoted to *s*-process element abundances in M-giant stars[1], mostly because of the complex analysis of such cool-star crowded spectra. Smith & Lambert (1985, 1986, 1988), Smith et al. (1987), Lambert (1991), Lambert et al. (1995) analysed a few hundred stars in total and found a correlation between the ^{12}C and *s*-process abundances at the AGB star surface, which is in agreement with model predictions, as both species are produced in the stellar interior. However, neutron sources in AGB stars, and especially in intermediate-mass stars (between ∼4 and $\sim 8\,M_\odot$), were still not fully understood at the time of these previous studies. For low-mass AGB stars, the main neutron source is the ^{13}C(α,n)^{16}O reaction. Nevertheless, when looking at the *s*-process element abundance distribution, some AGB stars show a flatter distribution than that of the solar distribution, and this led Danziger (1966) to suggest that much longer and/or larger density neutron exposures could occur in some AGB stars (Iben & Renzini 1983). In fact, for intermediate-mass AGB stars, the main neutron source is now known to be the ^{22}Ne(α,n)^{25}Mg reaction (Cameron 1960; Iben 1975; Käppeler et al. 2011). Due to its higher neutron density, AGB star atmospheres can then be enhanced in Rb, ^{25}Mg, and ^{26}Mg. However, some of these stars show no enhancement in Rb, and no Tc signatures[2] can be found that could be explained by the absence of a ^{13}C pocket (Lugaro et al. 2016). This result is theoretically predicted by Goriely & Siess (2004), Herwig (2004) via the so-called hot dredge-up (Straniero et al. 2023). Notably, some very specific studies concerning different sub-classes of AGB stars have brought some complementary information about the AGB yields. One could, for instance, cite CH-stars (Vanture 1992; Cristallo et al. 2016), Ba-stars (Cseh et al. 2022), and C-rich stars (Utsumi 1970; Abia et al. 2002), but the sample statistics were always rather small in all of these studies. Therefore, there is still a lack of very large samples of AGB stars with homogeneous *s*-process abundances that could be used to better understand the yield productions of oxygen-rich AGB stars[3].

In this context, the spectroscopic observations collected by the ESA *Gaia* mission are of particular interest. Indeed, thanks to the analysis of the *Gaia*/Radial Velocity Spectrometer (RVS) spectra by the General Stellar Parametrizer from Spectroscopy module (GSP-Spec; Recio-Blanco et al. 2023), chemo-physical parameters such as effective temperature ($T_{\rm eff}$), surface gravity ($\log(g)$), global metallicity ([M/H]), and enrichment in α-elements with respect to iron ([α/Fe]), as well as up to 13 individual chemical abundances, have been determined for 5.6 million stars, including a few hundred thousand AGB stars. Among the 13 chemical elements, three are formed via neutron-capture processes: zirconium ($Z = 40$), cerium ($Z = 58$), and neodymium ($Z = 60$). Although the Zr line found in the RVS domain is not formed in cool star spectra, the Ce and Nd lines are well detected in the spectra of a large number of AGB stars, which led to the publication of a large catalogue of *s*-process abundances in these evolved stars.

The goal of this article is to focus on the Ce and Nd abundances in AGB stars analysed by the GSP-Spec module. We recall that GSP-Spec cerium abundances in less evolved stars have already been presented in Contursi et al. (2023) in order to discuss the Galactic content and chemical evolution in this element. The present work is organised as follows. Section 2 presents the selection of the sample of AGB stars with high-quality Ce and Nd abundances, while Sect. 3 explores the general properties of this sample. We also include in this section a short overview of the Nd abundances in the Galactic Halo. We then discuss the observed content of Ce and Nd in AGB stars by comparing the observed content to predictions from AGB *s*-process models. Finally, the conclusions of this work are summarised in Sect. 5.

2. The GSP-Spec sample of asymptotic giant branch stars with *s*-process element abundances

Among the 5.6 million stars published within the *Gaia* DR3 catalogue (Gaia Collaboration 2023a), the GSP-Spec module (Recio-Blanco et al. 2023) has been able to derive abundances of two second-peak *s*-process elements. In total, one can indeed retrieve 103 948 and 55 722 stars with Ce and Nd abundances, respectively, whatever the stellar type is. This first sample of 55 722 Nd abundances is referred as the complete Nd sample, hereafter. These numbers include abundances derived in AGB stars but also in less evolved stars (see, for instance for Ce, Contursi et al. 2023). The scope of this section is to present the best working sample of these *s*-process element abundances for the best-parameterised AGB stars.

2.1. *Asymptotic giant branch stars parameterised by GSP-Spec*

We first highlight that the GSP-Spec module has published atmospheric parameters and chemical abundances from the analysis of the *Gaia*/RVS spectra ($R \sim 11\,500$). The individual chemical abundances have been estimated thanks to a specific grid of reference synthetic spectra and the GAUGUIN algorithm (Bijaoui 2012; Recio-Blanco et al. 2016) while considering Local Thermodynamical Equilibrium (LTE), solar abundances of Grevesse et al. (2007), and the atomic and molecular line data of Contursi et al. (2021).

---

[1] We recall that the atmosphere of these M-type stars is still oxygen-rich, as it was when they formed.

[2] Tc is a key element to prove the AGB nucleosynthesis as its isotope with the largest lifetime is ^{98}Tc that rapidly decays after about 4.2 Myr.

[3] Oxygen-richness being defined as C/O ratio smaller than unity.

Together with the parameters and individual chemical abundances, GSP-Spec also provides quality flags (flags_gspspec, hereafter) that are recommended in order to select the most accurate parameters, including abundances. These flags can either be related to the stellar parametrisation (induced, for instance, by possible biases caused by radial velocity uncertainties, flux noise, or rotational velocities) or to the derived chemical abundance of a given element. The corresponding flags for the abundances of an X species are XUpLim and XUncer. We note that the value "0" for all of these flags corresponds to the best measurements, and we refer to Recio-Blanco et al. (2023) for a more detailed description of these flags.

First, without considering any flag restriction and after applying the calibrations recommended by Recio-Blanco et al. (2023) for the atmospheric parameters[4], we found that among all the GSP-Spec parameterised stars, 174 104 of them have a published $T_{\rm eff} \leq 4000$ K and $\log(g) \leq 2.0$ (most stars cooler than $\sim$3650 K were disregarded for the DR3 analysis)[5]. These atmospheric parameter cuts were adopted in order to ensure the AGB nature of the selected stars, recently confirmed by their K-band absolute magnitude (see below). Then, we considered only the best-parametrised stars by (i) setting the first 13 flags equal to zero, except the extrapol flag, which is fixed to be $\leq$1, and (ii) selecting only stars with an $S/N > 100$ or a gof < -3.5[6]. These last two criteria are linked to the detection of the Ce and Nd in the analysed spectra (see Table C.9–C.11 of Recio-Blanco et al. 2023). Hereafter, the remaining 128 335 cool-giant stars are referred to as the "best-parameterised AGBs".

The top panel of Fig. 1 shows a Kiel diagram of these AGB stars colour-coded according to their mean metallicity. Noticeably, the more metal-poor stars are found to have smaller gravities. We also remark that there is a lack of stars around $T_{\rm eff} \sim 3730$ K. These biases result from the difficulty in parameterising more metal-rich and/or cooler AGB stars that have complex spectra crowded by molecular lines. This has been explored with the KMgiantPar flag (stars with a non-null value of this flag have set values of $T_{\rm eff}$ and $\log(g)$, see Recio-Blanco et al. 2023). In order to reject such complex cases, we remind that we adopted for the selection criteria KMgiantPar = 0.

To confirm the AGB nature of the best-parameterised AGBs, we estimated their absolute K magnitude value (M_K). For that purpose, we adopted their apparent 2MASS K-band photometry Skrutskie et al. (2006) and the photo-geometric distances from Bailer-Jones et al. (2021). We then computed the absolute K-magnitude for 120 032 stars (93.5% of the whole sample) using a re-normalised unit weight error (RUWE) smaller than 1.4 and an astrometric fidelity factor for their astrometric solution (fidelity_v2) larger than 0.5 (Rybizki et al. 2022), assuring a good *Gaia* astrometric solution. We note that following this procedure, we neglected the interstellar extinction and thus actually derived a lower limit of the real M_K (the stars are actually brighter than our estimate). We found that about 89% of our stars are brighter than $M_K < -4$. This confirms well the AGB nature of the sample according to Abia et al. (2022), who showed in their *Gaia*-2MASS diagrams that AGB stars are typically brighter than $M_K \sim -4$ to -5 mag (taking into account the interstellar medium absorption and their intrinsic *Gaia* and 2MASS colours). We note that considering extinction only would make the stars a bit brighter, and the resulting sample would probably contain a larger fraction of AGB stars than the current one. However, we cannot completely exclude that our sample may be polluted by some extrinsic S-stars, CH-stars, R-stars[7], or early-AGB stars, which would have similar M_K magnitudes (Abia et al. 2022). Such stars may not be enhanced in s-process elements and may introduce some dispersion in the observed [Ce/Fe] and/or [Nd/Fe] ratios with possibly negative values.

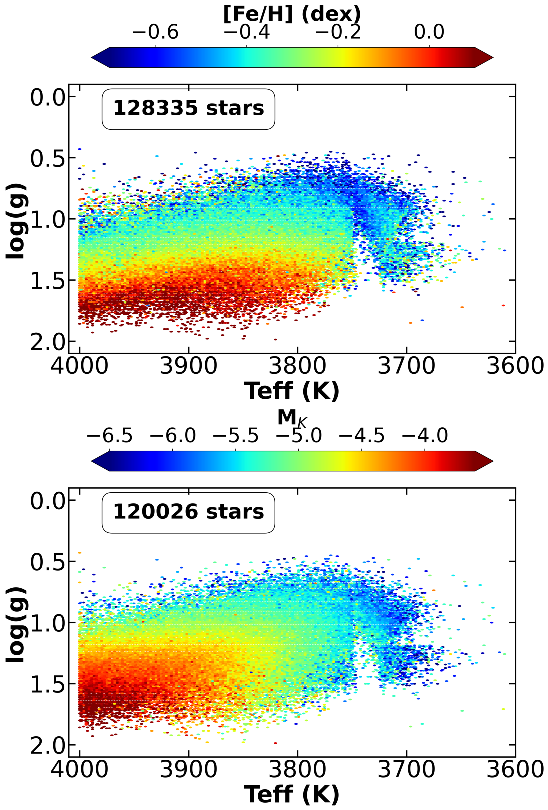

Fig. 1. Kiel diagram of the best-parametrised GSP-Spec AGB stars colour-coded by their metallicity (top panel) and their absolute K magnitude (neglecting the extinction; bottom panel). This figure uses the calibrated $\log(g)$ and [M/H] as recommended by Recio-Blanco et al. (2023).

The bottom panel of Fig. 1 shows a Kiel diagram of the best-parameterised AGB colour-coded according to their absolute K magnitude. It can be seen that cooler stars have lower gravities and larger M_K, again confirming their AGB nature. Finally, we note that 97% of the working sample of AGB stars with Ce and Nd abundances (best-parameterised AGB stars defined below) have $M_K < -4$ mag (the other 3% having $M_K < -3.2$ mag), confirming their AGB nature.

2.2. High-quality GSP-Spec cerium and neodymium abundances in asymptotic giant branch stars

Among the best-parameterised AGB, GSP-Spec derived Ce and Nd abundances for 46 144 and 34 838 of the stars, respectively (without any abundance flag filtering). As the aim of this study is to analyse the largest sample with the most accurate chemical

---

[4] See also `https://www.cosmos.esa.int/web/gaia/dr3-gspspec-metallicity-logg-calibration`

[5] We adopted the median value of the published parameters here.

[6] The gof corresponds to the goodness-of-fit for the observed spectrum over the entire RVS spectral range.

[7] The R-star spectra could be very similar to the O-rich early-AGB or M-stars.

abundances, we present a specific flag combination to build high-quality Ce and Nd working samples in the following sections.

2.2.1. Cerium

The description of the cerium line analysed by GSP-Spec and the associated sample of Ce abundances have already been presented in Contursi et al. (2023). Briefly, high-quality Ce abundances were retained only if (i) Ce abundance uncertainties were smaller than 0.2 dex; (ii) vbroad $\leq 13\,\mathrm{km\,s^{-1}}$; (iii) the abundance flags were set at CeUpLim ≤ 2 and CeUncer ≤ 1; (iv) extrapol ≤ 1; and (v) KMgiantPar ≤ 1 if gof < -3.75. We highlight that the vbroad parameter provides information on the line broadening (rotational velocity, macroturbulence, etc.), whereas extrapol indicates if the GSP-Spec atmospheric parameters are extrapolated beyond the reference grid limits. (We refer the reader to Contursi et al. 2023; Recio-Blanco et al. 2023 for a complete description of the choice of these adopted filters). We also note that calibrating these Ce abundances was found to be unnecessary (see the discussion in Contursi et al. 2023). In the following, we only kept the best-parameterised AGB with the best Ce abundance as defined above, leading to a working sample of 17 765 AGB stars with high-quality cerium abundances (referred to as the Ce AGB sample hereafter). We note that the Ce abundances of this sample vary from −0.17 to 1.10 dex and that no higher Ce abundances were found due to the cut in T_{eff}. We also recall that the *s*-process contribution for Ce is about 80% at the Solar System formation epoch (Arlandini et al. 1999; Bisterzo et al. 2016; Prantzos et al. 2018, 2020).

2.2.2. Neodymium

Neodymium abundances were estimated from one single line of Nd II located at 859.389 nm in the vacuum (859.153 nm in the air)[8]. Its lower-level excitation energy and oscillator strength was fixed to 1.357 eV and −1.650, respectively (Den Hartog et al. 2003). We recall that neodymium has seven stable isotopes: ^{142}Nd (27.13%), ^{143}Nd (12.18%), ^{144}Nd (23.80%), ^{145}Nd (8.30%), ^{146}Nd (17.19%), ^{148}Nd (5.76%), and ^{150}Nd (5.64%; Den Hartog et al. 2003). All of these isotopes were considered in the computation of the reference synthetic spectra. The *s*-process contribution for Nd is about 60% (Arlandini et al. 1999; Bisterzo et al. 2016; Prantzos et al. 2018, 2020). Finally, we note that this Nd line has not been astrophysically calibrated by Contursi et al. (2021) because of a lack of high-quality Nd abundances in reference stars. It could be slightly blended for some specific combinations of atmospheric parameters and chemical abundances by a weak CN line, but thanks to checks with synthetic spectra, this contribution has been found to be negligible for stars cooler than 4000 K (as long as the stellar atmosphere is not enhanced in carbon; see Sect. 3.1). This Nd line could also be slightly blended by some weak TiO lines in rather metal-rich stars cooler than 4000 K. However, as O and Ti are both considered α-elements, the TiO contribution is expected to be rather well modelled in the reference synthetic spectra as [α/Fe] abundances are determined by the GSP-Spec pipeline before the estimation of the individual abundances (Ti and O abundances being assumed to vary in lockstep with [α/Fe]).

As already presented by Contursi et al. (2023) for cerium, we illustrate in Fig. 2 the smallest Nd abundance (in dex) that could be measured for metallicities varying between −1.0 to 0.0 dex in a Kiel diagram. As expected, the Nd line is easier to detect in AGB stars (as far as [Nd/Fe] $\gtrsim$ 0.4 dex) than in dwarf stars (much higher Nd abundances are required to possibly detect this line).

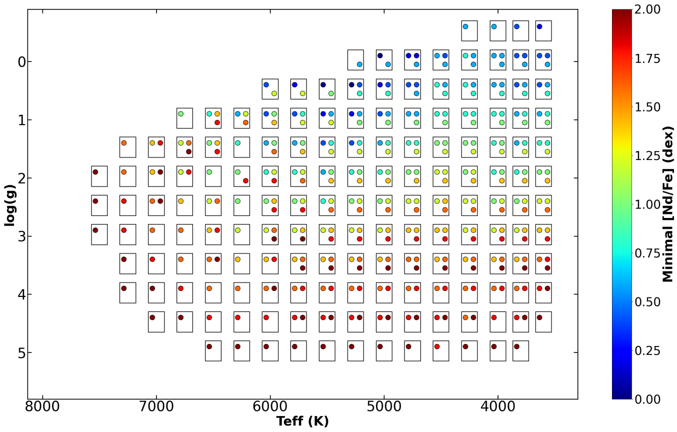

Fig. 2. Kiel diagram colour-coded with the lowest neodymium abundance (in dex) that could be detected in a spectrum whose (normalised) line centre flux is 0.5% deeper than that of a reference spectrum computed with [Nd/Fe] = −2.00 dex. For each combination of effective temperature and surface gravity, each small square contains the estimate of the lowest Nd abundance for three values of [M/H]: 0.0, −0.5, and −1.0 dex (from top to bottom and left to right).

We built a sub-sample of AGB stars with the most accurate Nd abundances by applying the best combination of the flags_gspspec, following a similar procedure as for Ce. We note that setting all flags_gspspec equal to zero (including those related to the neodymium abundances) resulted in a sample of five stars only. This number can be substantially increased while maintaining a high quality for the Nd abundances by relaxing some of the flags_gspspec. For example, to build our working sample, we applied the same flag combination as for the low-uncertainty Ce sample (see Sect. 2.2.1). We note that we also kept stars with [Nd/Fe] $\geq$ 2.00 dex (abundance upper limit caused by border effects of the reference spectra grid) if their KMgiantPar = 0 and NdUpLim = 0. For these stars, we adopted [Nd/Fe] = 2.00 dex in the following, although their abundances could be higher. Our final working sample was then composed of 3492 AGB stars with high-quality Nd abundances and is referred to as the Nd AGB sample. An example of the ADQL query to retrieve this sample can be found in Appendix A.

As a validation check of the quality of these selected abundances, we looked for Nd abundances for our Nd AGB sample stars in the literature. We found only a few stars in common with previous studies since none were exclusively devoted to AGB stars. We have six stars in common with Tautvaišienė et al. (2021; mainly FGK-type stars) and nine in common with Hayes et al. (2022). Unfortunately, of these 15 stars, only nine of them have literature atmospheric parameters close enough to ours to allow for a proper comparison of the Nd derived abundances (adopting differences in T_{eff}, log(g), and [M/H] smaller than 150 K, 0.50, and 0.30 dex, respectively). Although our Nd abundances seemed to be systematically larger than the few found in the literature, we decided not to calibrate them using a comparison sample due to the small number of stars. Nevertheless, as our sample is composed of giant stars only, we analysed the observed spectrum of Arcturus (Hinkle et al. 2000) with the GSP-Spec pipeline in order to estimate its Nd abundance, adopting the atmospheric parameters of Contursi et al. (2021). As the rather larger GSP-Spec [Nd/Fe] in Arcturus was confirmed with

---

[8] The conversion between air and vacuum wavelength was made using the Birch & Downs (1994) relation.

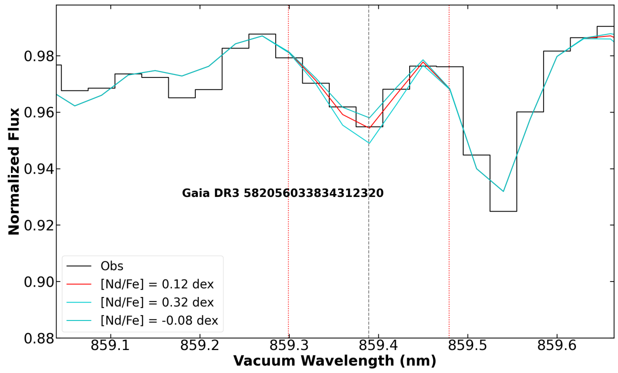

Fig. 3. Comparison around the Nd II line between the RVS public spectrum of *Gaia* DR3 582056033834312320 (in black) and a model spectrum computed from its GSP-Spec parameters (in red). The cyan lines show synthetic spectra with Nd abundance ±0.2 dex around the adopted Nd abundance. The calibrated parameters of this star are $S/N = 1110$, $T_{\rm eff} = 3825$ K, $\log(g) = 0.37$, $[\rm Fe/H] = -0.74$ dex, $[\alpha/\rm Fe] = 0.12$ dex, $[\rm Nd/Fe] = 0.12$ dex, and $[\rm Ce/Fe] = 0.14$ dex.

respect to the value reported by Fanelli et al. (2021; who adopted similar atmospheric parameters as us), we forced our [Nd/Fe] in Arcturus to be equal to theirs ($[\rm Nd/Fe] = -0.03$ dex in the Grevesse et al. 2007 solar scale) and calibrated all the other Nd abundances accordingly.

Finally, to illustrate the GSP-Spec analysis of these Nd AGB sample stars, we show in Fig. 3 a comparison between the *Gaia*/RVS public spectrum and its associated synthetic spectrum, computed using the GSP-Spec atmospheric parameters and chemical abundances, for a star representative of the Nd AGB sample. As can be seen, there is an excellent agreement between the observed (in black) and modelled spectra (in red), confirming the good determination of Nd abundances in the AGB stars of our sample.

3. Global properties of the *s*-process asymptotic giant branch star sample

We describe in this section the properties of the *s*-process AGB sample which is composed of the 17 765 and 3492 stars (the Ce AGB sample and Nd AGB sample, respectively). As 1713 of these stars have both Ce and Nd abundances, the *s*-process AGB sample is actually composed of 19 544 stars.

3.1. Stellar types and oxygen-rich nature

In Sect. 2.1, we confirmed the AGB nature of the 19 544 stars that compose the *s*-process AGB sample thanks to an estimation of their absolute magnitude in the *K*-band. Moreover, 445 of these stars have been classified as long-period variables (LPVs) by Lebzelter et al. (2023) thanks to *Gaia*/DR3 photometric epoch observations, leading to an independent confirmation of the AGB nature for a couple of them. Their mean period is ~95 days, and the longest periods reach ~600 days (*Gaia*/DR3 data favour the detection of LPVs with the shortest periods).

We looked for the stellar type of the *s*-process AGB sample stars. In particular, we were interested in their possible atmospheric enrichment in carbon resulting from the dredge-up events characterising this specific stage of the evolution of low- and intermediate-mass stars. The presence of carbon (C-rich) stars in this sample could be problematic since their chemical analysis has been performed by assuming oxygen-rich stellar atmospheres and a solar-scaled C/O ratio within the GSP-Spec module. This may slightly modify the stellar parameters and associated chemical abundances if different C/O ratios are adopted. In any case, the search for C-rich stars was first conducted by checking the cnew_gspspec parameter, which is an indicator of a possible CN enrichment (or impoverishment) in the stellar atmosphere (C-rich star spectra are characterised by the presence of a strong CN line analysed by GSP-Spec). (We direct the reader to Recio-Blanco et al. 2023 for a complete definition of this CN-parameter). Among the 19 544 stars that comprise our sample, 13 873 of them have a published cnew_gspspec value, and all of the stars in this subset have this parameter close to zero, indicating that they have a close-to-solar CN abundance. Thus, they are not enriched in CN, and this confirms their likely oxygen-rich nature.

We also searched for possible carbon stars by looking at the C-rich flag proposed by Lebzelter et al. (2023), which led to a list of about half a million LPV candidates possibly enriched in carbon. Only 14 stars among the 19 544 of our sample could be suspected as being carbon rich. However, this number should be considered with caution since this C-rich flag could lead to erroneous detection (see Messineo 2023, who reported about 1% of false detections, and see also the discussion in Sanders & Matsunaga 2023). Nonetheless, we also cross-matched our sample with the list compiled by Abia et al. (2022), who examined the characteristics of already well-known Galactic carbon stars by using *Gaia* eDR3 data. These authors also presented a catalogue of about 2700 new Galactic carbon star candidates. None of our stars were found to be carbon-rich according to this compilation, but 18 of them are already known to be of spectral type *S* (i.e. their C/O ratio is close to unity, but they are still oxygen-rich).

Finally, we show the Nd AGB sample in the *Gaia*-2MASS diagram (Fig. 4) colour-coded with the metallicity (left panel) and the Nd abundance (right panel). This figure allowed us to independently confirm the O-rich nature of our sample stars. We obtained a very similar figure for the Ce AGB sample. This diagram shows the absolute *K* magnitude with respect to a particular combination of the *Gaia* and 2MASS photometry expressed through the reddening-free Wesenheit function (Soszyński et al. 2005), defined as $W_{\rm RP,BP-RP} = G_{\rm RP} - 1.3\,(G_{\rm BP} - G_{\rm RP})$ and $W_{K,J-K} = K - 0.686\,(J - K)$ by Lebzelter et al. (2018). As can be clearly seen, almost all the stars of this sample are located outside the C-rich regime, confirming their O-rich nature. Several of the stars also appear slightly fainter than typical AGB stars, but this can be explained by the neglected extinction when computing their absolute magnitude. We remark that this *Gaia*-2MASS diagram provided a hint regarding the stellar masses being in the low-mass regime. This is discussed later in Sect. 4. Finally, based on these checks, we were confident about the real oxygen-rich and AGB nature of the *s*-process AGB sample, thus strengthening the quality of their *s*-element abundance determination.

3.2. Kinematical and dynamical properties

The kinematical and dynamical properties of the *s*-process AGB sample were explored using their Cartesian stellar coordinates, Galactocentric radii, and cylindrical velocities, adopted from Gaia Collaboration (2023b), and the orbital parameters (such as $Z_{\rm max}$ and eccentricity) are from Palicio et al. (2023)[9].

---

[9] These parameters can be found in the table performance verification/gaiadr3.chemical_cartography in the *Gaia* archive (`https://gea.esac.esa.int/archive/`).

A majority of the s-process AGB sample exhibits disc properties, as 81% of the stars have $|Z_{\rm max}| < 1$ kpc, and about 88% of our sample present eccentricities smaller than 0.25. The highest eccentricity values correspond to the lowest metallicities ([M/H] < -0.70 dex), hence the highest Ce and Nd abundances (see Fig. 5; commented in the next subsection). Finally, about 88% of the stars present a total velocity (quadratic sum of their three velocity components) smaller than 80 km s^{-1}, confirming that the majority of the s-process AGB sample exhibits disc kinematical properties.

3.3. Chemical properties

In this section, we present the s-process abundances of these stars. We first focus separately on the Ce AGB sample and Nd AGB sample and then on the sub-sample of AGB stars that have both Nd and Ce abundances.

Figure 6 shows the Kiel diagrams for the Ce AGB sample (upper panel) and Nd AGB sample (lower panel) colour-coded according to the stellar counts (left panels) and the metallicity (central panel). We remark that the metallicity of our sample stars decreases with decreasing log(g). This observational bias is a general feature of the GSP-Spec sample of AGB stars, as already discussed above (see Fig. 1 and associated text). The right panels show the Kiel diagrams colour-coded based on Ce (upper panel) and Nd abundances (lower panel). Noticeably, at a constant metallicity (hence a rather constant log(g)), the neodymium and cerium abundances are found to be larger for cooler and more luminous stars. Such features can also be observed when looking at the second and last columns of Fig. 5, which present the Ce (top panel) and the Nd abundances (lower panel) with respect to the metallicity colour-coded according to $T_{\rm eff}$ and M_K, respectively. This can also be confirmed by looking at Fig. 4, where larger Nd abundances are found for more luminous stars. This is expected from AGB star evolution. Indeed, the successive TDUs characterising this evolutionary phase bring the material formed within the He-intershell towards the surface and hence change the composition of the envelope. Initially enriched in O, the envelope becomes richer in s-process elements and primary carbon, which increases the radiative opacity and thus causes important changes in the physical structure of the AGB envelope. This impacts the stellar radius, luminosity, mass loss, and effective temperature as well as the formation of molecular species such as CN, HCN, and C_2 (Marigo 2002; Cristallo et al. 2009). At a given metallicity and log(g), a cooler AGB has experienced more TP (hence more TDU) than when it was less evolved on the AGB and thus was slightly hotter, leading to an envelope more enriched in s-process elements, as can be seen in Fig. 6.

We also investigated the correlation between the Ce AGB sample and the Nd AGB sample. We found 1713 stars that have both high-quality Nd and Ce abundances. As can be seen in Fig. 7, a high positive correlation was found between these two chemical species (Pearson correlation coefficient = 0.75)[10]. The associated dispersion is rather large since it is dominated by the Nd measurement uncertainties because the Nd II line is more difficult to analyse. Such a correlation again confirms the quality of the derived abundances since it is actually expected, as both elements belong to the s-process second peak and hence have a similar nucleosynthetic origin. We also remark that colour-coding this correlation with $T_{\rm eff}$ clearly showed the enhancement of the Ce and Nd abundances for cooler stars (i.e. for more evolved stars on the AGB), as illustrated in Figs. 6 and 5.

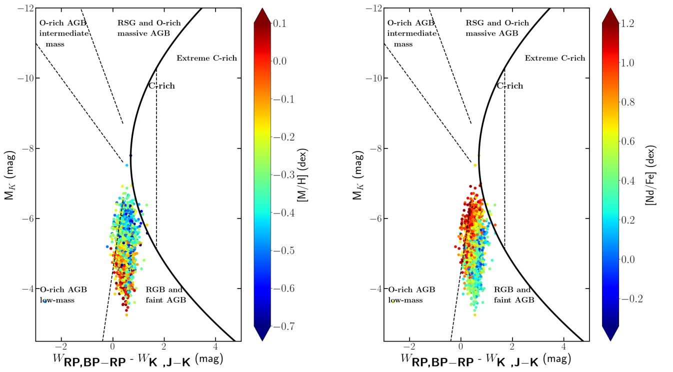

Fig. 4. *Gaia*-2MASS diagram for the Nd AGB sample colour-coded with metallicity (left panel) and Nd abundance (right panel). The curved line delineates the theoretical limit between O-rich (left-side) and C-rich AGB stars (right-side). The dashed lines separate sub-groups of stars as indicated in the figure.

3.4. Neodymium in the Galactic halo

Even though the majority of the Nd AGB sample seems to belong to the disc, a small fraction of these stars belong to the Galactic halo. Following the same procedure as in Gaia Collaboration (2023b), we therefore investigated neodymium abundances in stars belonging to the halo component of the Milky Way (accreted systems and globular clusters). We note that a similar study for cerium in halo stars has already been presented in Contursi et al. (2023).

First, no stars in common were found by cross-matching the globular cluster compilation of the Harris catalogue (Harris 1996) with the Nd AGB sample. Nevertheless, we found one star (ID = 1821609090431019392) belonging to the M71 globular cluster when cross-matching with the lower-quality complete Nd sample (we reiterate that this sample corresponds to the 55 722 stars having Nd abundances but without any flag restriction).We used a maximum separation in the sky of 0.5° and checked that the radial velocity of the stars was compatible with that of M71, with a difference lower than 0.5 km s^{-1} compared to the value estimated by Baumgardt & Hilker (2018). The (calibrated) metallicity of this one star ([M/H] = -0.72 ± 0.05 dex) is compatible with the M71 literature estimates (-0.82 dex found in Carretta et al. 2009 and -0.80 dex found in Boesgaard et al. 2005). The atmospheric parameters of this star are also very compatible with the estimates of Sneden et al. (1994), Gerber et al. (2020), with mean $T_{\rm eff}$ and log(g) differences of 70 K and 0.22 dex, respectively. We found an Nd abundance of 0.95 ± 0.22 dex, while no abundance of Ce has been found for this star. This value is higher than the mean [Ce/Fe] of M71 found in Masseron et al. (2019; 0.27 dex) and the mean [Ba/Fe] (0.34 dex) and [La/Fe] (0.20 dex) found in Ramírez & Cohen (2002). The difference could be caused by the AGB nature of this specific star, which may not be fully representative of the Nd abundance of this globular cluster and has an atmosphere already well enriched in s-elements.

We also explored the *Gaia* DR3 Nd abundances of accreted systems, which have been identified as overdensities in the energy versus vertical angular momentum (E–L_z) diagram in Gaia Collaboration (2023b). As no star was found to belong to any accreted system in the Nd AGB sample, we again

---

[10] We note that there is a star that has [Nd/Fe] = 0.23 dex and [Ce/Fe] = 0.80 dex. This outlier star is identified as "S-Star".

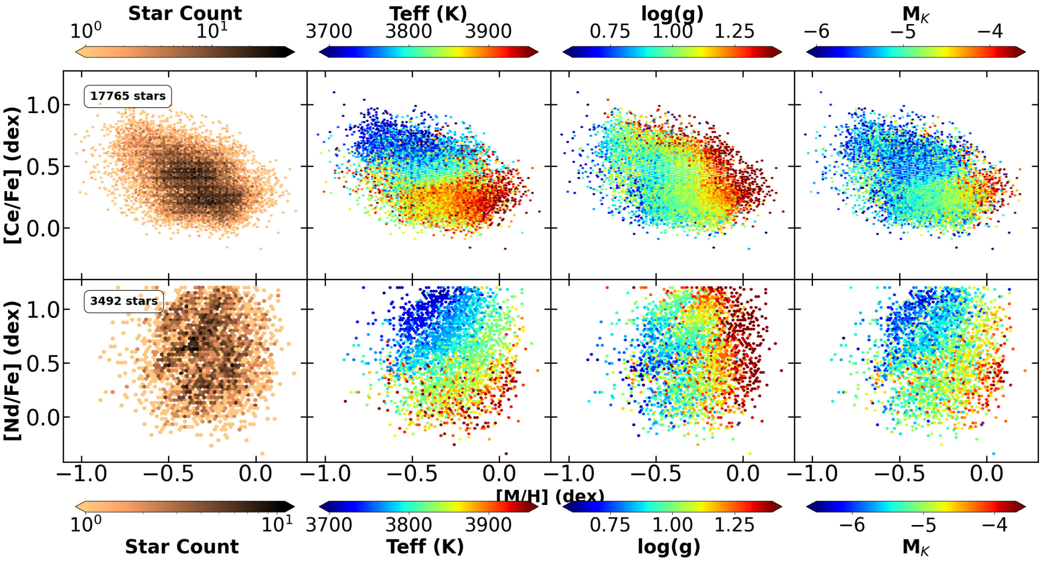

Fig. 5. Top panels: with respect to metallicity, [Ce/Fe] colour-coded by (from left to right) stellar count, $T_{\rm eff}$ log(g) and M_K. Bottom panels: same as top panels but for Nd abundances.

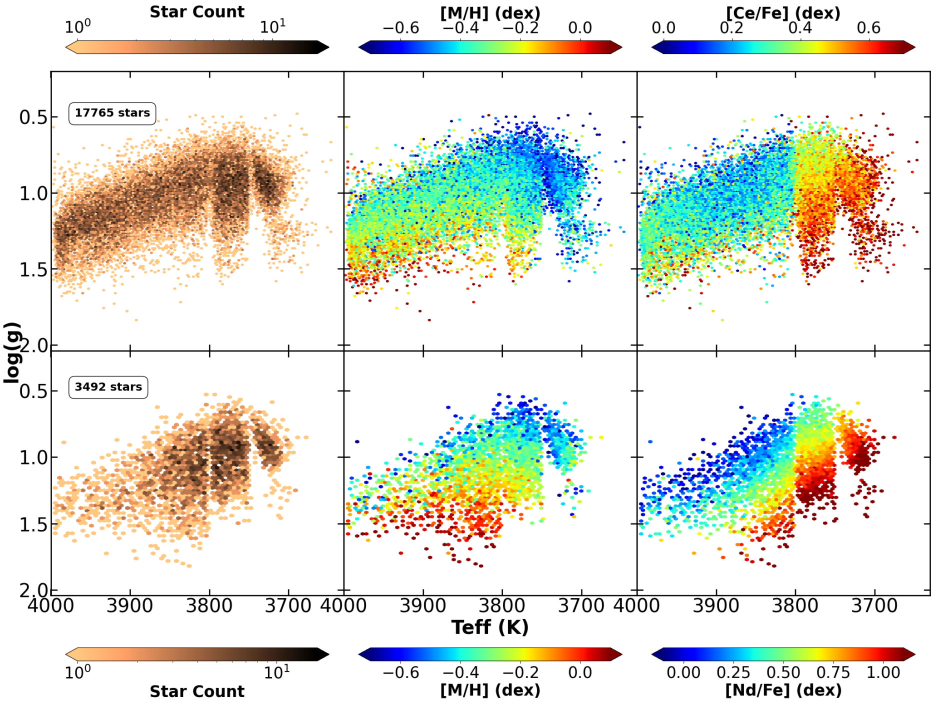

Fig. 6. Kiel diagrams of the Ce AGB sample (top panels) and the Nd AGB sample (bottom panels). From left to right, the samples are colour-coded according to the stellar count, the metallicity, and the corresponding s-process abundance. We note that this figure is an hexbin plot.

investigated the complete Nd sample and rejected all stars with a KMgiantPar value larger than unity as well as all non-zero values for all parametrisation flags. We found one star in Thamnos (Koppelman et al. 2019; Helmi 2020), four stars in the Helmi stream (Helmi 2020), one in Sequoia, (Myeong et al. 2019) and one in the Gaia-Enceladus-Sausage (GES; see Helmi et al. 2018; Belokurov et al. 2018; Myeong et al. 2018; Feuillet et al. 2020, 2021). No chemo-physical literature studies were found for those stars except for one in the Helmi stream (ID = 1591836174070974592), whose atmospheric GSP-Spec parameters are close to that of Jönsson et al. (2020; difference in $T_{\rm eff}$, log(g), [M/H], [α/Fe] = 31 K, 0.32, 0.18 dex, and 0.02 dex, respectively (though no Ce abundance was provided). In order to investigate the accreted nature of the seven stars, we kept only candidate stars with [M/H] < −0.7 dex or with a low [Ca/Fe] ([Ca/Fe] < 0.3 dex), similar to the procedure adopted by Contursi et al. (2023). This selection removed three of the stars identified as Helmi stream members. This misidentification is due to the proximity of the Helmi stream to the solar neighbourhood in the (E−Lz diagram). Table 1 shows the *Gaia* DR3 Id and the corresponding accreted system of the four remaining stars as well as their atmospheric parameters and Nd and Ce abundances.

As can be seen in Table 1, the metallicity of the stars belonging to the GES and Helmi systems are similar, as already found in Contursi et al. (2023). We remark that the table shows a much lower metallicity for the star belonging to the Sequoia system compared to that of the three other accreted systems. A lower mean metallicity for Sequoia than

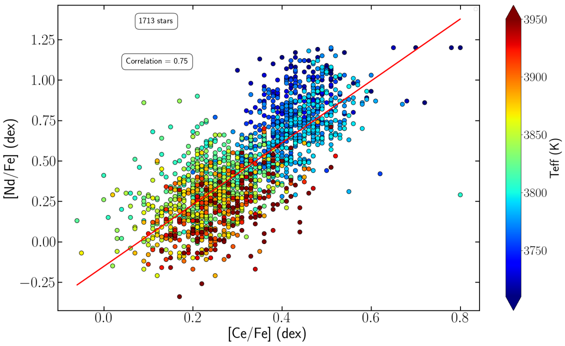

Fig. 7. Correlation between Ce and Nd abundances for AGB stars found in both the Ce AGB sample and Nd AGB sample, colour-coded by their $T_{\rm eff}$. The slope of the red line is 1.91, while the standard deviation is 0.44 dex. The Pearson correlation coefficient is also reported.

for GES was already found in Feuillet et al. (2021). We also found a rather high [Ca/Fe] abundance for the star belonging to the Sequoia system. Even though smaller [Mg/Fe][11] abundances have been found in Sequoia than in GES by Matsuno et al. (2022), Feuillet et al. (2021) found high-[Mg/Fe] stars belonging to Sequoia system. Moreover, we remark that the star belonging to GES presents a higher [Nd/Fe] value than that of the Helmi stream ([Nd/Fe] = 0.83 dex), Sequoia system ([Nd/Fe] = 0.35 dex), and Thamnos ([Nd/Fe] = 0.27 dex). As already suggested by Recio-Blanco et al. (2021) with [Y/Fe] and Contursi et al. (2023) with [Ce/Fe] measurements, a higher value of [Nd/Fe] may suggest a higher mass of the system progenitor. This follows the mass estimations of these accreted systems by Koppelman et al. (2019). We note that Matsuno et al. (2022) also found a higher abundance for the s-process elements (Y and Ba) in GES than in Sequoia. Finally, we note that the cerium abundance of the star from the Thamnos system would suggest a similar mass of the progenitor as that of the Helmi stream. However, it is important to note that for the Thamnos and Helmi stream stars, the estimated [Nd/Fe] and [Ce/Fe] are compatible within error bars. However, our suggestions are based on only one star and should be taken carefully because of the adopted Ce and Nd flags_gspspec. It is also important to note that this star of the Helmi stream may not be fully representative of the chemistry of the stream due to its AGB nature (since it is actually a producer of Nd).

4. Constraints to asymptotic giant branch star yield and evolutionary models

The s-process AGB sample presented above has a unique set of abundances that allow the evolution of low- and intermediate-mass stars on the AGB to be constrained. In particular, their yields for second-peak s-elements and their role in the Galactic chemical evolution of these species can be explored. In this section, we compare our abundances with yields predicted by the FRUITY[12] (Cristallo et al. 2009, 2011, 2015) and Monash models (Lugaro et al. 2012; Fishlock et al. 2014; Karakas & Lugaro 2016; Karakas et al. 2018). These two sets of models are the most complete in terms of explored masses and metallicities, and they allow for a useful discussion of the impact of their different physical assumptions that could affect their yield predictions.

4.1. FRUITY and Monash models

The FRUITY (FUNS Repository of Updated Isotopic Tables and Yields) models are computed by simultaneously considering both stellar evolution and nucleosynthesis. In these models, the ^{13}C pocket is formed in a self-consistent way, and its mass is linked to an exponential decaying velocity function that includes a free overshoot parameter β. This parameter is set to maximise the ^{13}C pocket and hence the s-process element production. Time-dependent convective overshoot at the base of the envelope is also included. We considered only non-rotating FRUITY models (as our stars all have vbroad < 13 km s^{-1}). We also adopted FRUITY models with a "standard" ^{13}C pocket. In order to cover the metallicity range of the s-process AGB sample, we considered five metallicities (Z = 0.002, 0.003, 0.006, 0.010, and 0.014, corresponding to [M/H] = −0.85, −0.67, −0.37, −0.15, and 0.00 dex, respectively) and eight masses (1.30, 1.50, 2.00, 2.50, 3.00, 4.00, 5.00, and 6.00 $M_\odot$)[13].

The Monash model nucleosynthesis was computed using a post-processing calculation based on the evolutionary models of Karakas & Lattanzio (2014). They include an exponentially declining profile of proton abundance in the top layers of the He-intershell rather than directly including proton mixing into the He-intershell (as done in the FRUITY models). We recall that this proton ingestion has a capital impact on the formation of the ^{13}C pocket (hence the s-process surface abundances), as these protons are captured by the present ^{12}C to form ^{13}C. Therefore, the size of the ^{13}C pocket in the Monash models is linked to a $M_{\rm mix}$ parameter (defined as the mass of protons that are partially mixed over a mass extent in the He-intershell). For each Monash model mass and metallicity, we adopted the standard values of $M_{\rm mix}$ provided in Tables 2 and 3 of Karakas & Lugaro (2016). We note that no rotation nor magnetic fields are included in these predictions. For comparison with the observed abundances, we considered three metallicities (Z = 0.0028, 0.007, and 0.014, corresponding to [M/H] = −0.70, −0.30, and 0.00 dex, respectively) and the same masses as for FRUITY, except that for Monash, the lowest considered masses were 1.0 and 1.25 $M_\odot$ (and not 1.3 $M_\odot$).

We note that in both sets of models, the mixing-length theory of convection was used, and no convective overshoot was implemented before the AGB phase. The computations were stopped when the envelope reached a critical mass, but the adopted mass-loss relations differ. Finally, we note that these codes do not assume the same solar abundances: FRUITY adopts the solar scale of Lodders (2003), whereas Monash models are based on Asplund et al. (2009) solar abundances. In order to compare their predictions to our data, we scaled them to the solar abundances of GSP-Spec abundances (Grevesse et al. 2007).

4.2. Cerium abundances as a proxy of the s-process content

When stars start their AGB phase and before the first TDU episode, the Ce and Nd abundances are not affected by previous dredge-up events. These species are thus still scaled to the solar ones (i.e. [Nd/Ce] = 0 dex). The successive TDU then enrich the AGB atmosphere in both elements. We investigated the evolution of this [Nd/Ce] ratio along the AGB using the prediction of the FRUITY and Monash models in order to check if the abundances of both elements remain close to each other. Thus, we show in Fig. 8 the [Nd/Ce] ratio predicted by both models at the surface of AGB stars of different masses and metallicities

---

[11] Mg and Ca both being α-elements.

[12] This is available online via: `http://fruity.oa-teramo.inaf.it`

[13] No lower masses are available.

Table 1. Signal-to-noise (S/N), $T_{\rm eff}$, log(g), [M/H], [Ca/Fe], [Nd/Fe], and [Ce/Fe] (and their associated uncertainties) for the four candidate accreted stars.

Gaia DR3 Id	System	S/N	$T_{\rm eff}$ (K)	log(g)	[M/H] (dex)	[Ca/Fe] (dex)	[Nd/Fe] (dex)	[Ce/Fe] (dex)
2410346779070638720	GES	68	4846	2.02	−0.98	0.16	1.12 ± 0.24	–
1591836174070974592	Helmi	101	3806	0.95	−0.73	0.37	0.73 ± 0.21	0.57 ± 0.20
5282079908816150912	Sequoia	407	4407	1.32	−1.53	0.47	0.25 ± 0.19	0.36 ± 0.20
1294315577499064576	Thamnos	657	4309	1.51	−1.01	0.27	0.17 ± 0.19	0.56 ± 0.08

Notes. We note that the log(g) and [M/H] and [Ca/Fe] were calibrated according to Recio-Blanco et al. (2023).

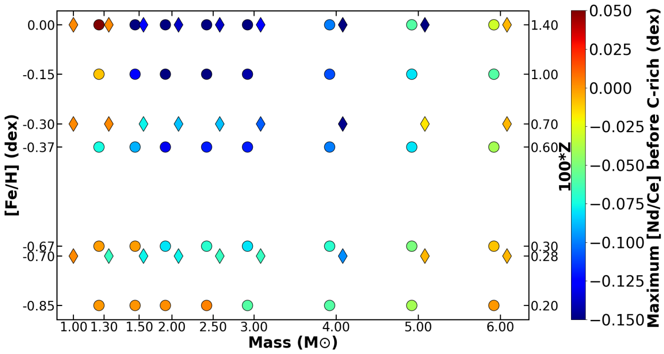

Fig. 8. Neodymium/cerium production predicted by the FRUITY (filled circles) and Monash models (filled diamonds) as a function of stellar mass and metallicity. The colour code corresponds to the maximum [Nd/Ce] production just before stars can become carbon-rich.

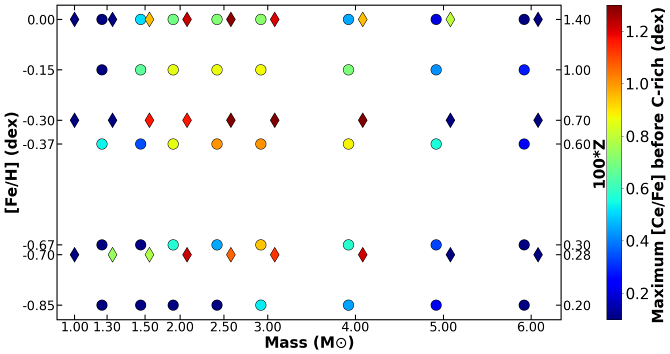

Fig. 9. Same as Fig. 8 but for [Ce/Fe] predicted abundances.

before their atmosphere could become carbon-rich. This corresponds to the largest predicted Nd and Ce enrichments in an O-rich AGB. As can be seen for both sets of models, the absolute value of the maximum [Nd/Ce] ratio before becoming a C-rich AGB stays within 0.15 dex whatever the masses and metallicities are. This illustrates the rather constant [Nd/Ce] production rate in different types of AGB stars. This therefore confirms the correlation found observationally between both elements (see Fig. 7 and associated text). We thus decided to focus only on Ce hereafter in order to avoid having our conclusions become blurred by the larger uncertainties associated with our Nd abundances. Moreover, this allowed our results for Ce to also be valid for Nd.

4.3. *Asymptotic giant branch star model prediction of s-process element enrichment*

In order to explore the atmosphere enrichment in s-process elements along the AGB, we show the maximum [Ce/Fe] abundance ratio of an oxygen-rich AGB in Fig. 9 in a similar way as in Fig. 8. We remark that for both sets of models, AGB stars of initial masses between 2 and 4 $M_\odot$ and metallicities between −0.80 dex and −0.10 dex present the largest Ce enrichment at their surface, exceeding [Ce/Fe] ~ 0.70 dex.

Briefly, we recall that for such masses (though this also applies to lower ones), second-peak s-process elements (such as Ce and Nd) are produced in the AGB interiors, within the so-called He-intershell (mainly composed of He and ^{12}C). Successive penetrations of the convective H-rich envelope (the so-called TDU) in this layer bring the material formed in the He-intershell towards the surface, drastically changing the envelope chemical composition. During the interpulse, protons left by the receding convective envelope are captured by the ^{12}C present in the He-intershell. This produces ^{13}C through the ^{12}C(p,γ)^{13}N($\beta^+\nu$)^{13}C reaction and forms the so-called ^{13}C pocket. This ^{13}C is then converted into ^{16}O through the ^{13}C(α,n)^{16}O reaction and provides an important quantity of neutrons that finally activate the s-process production (Straniero et al. 1995)[14]. We note that ^{14}N and ^{22}Ne pockets are also formed and partially overlap the ^{13}C pocket. As ^{14}N is a neutron poison, because of the ^{14}N(n,p)^{14}C reaction, the s-process nucleosynthesis occurs in the more internal tail of the ^{13}C pocket, where the amount of ^{14}N is low (Cristallo et al. 2009). All the elements formed in the He-intershell are brought up in the convective envelope by the subsequent TPs and TDUs. Moreover, the TDU has its maximum efficiency for this mass range between 2 and 4 $M_\odot$ (Cristallo et al. 2015). As already noticed by Cristallo et al. (2011), we also highlight that since intermediate-mass AGB stars have the largest production of Ce, they should make a large contribution to the interstellar medium enrichment, especially those with a mass around 2 $M_\odot$, because they are also more numerous and thus provide a good balance between the initial mass function of the Galaxy and the AGB Ce production rate (Karakas & Lugaro 2016).

We also note that although their global conclusions about Ce production are rather close, it can be seen that Monash models (at any mass and metallicity) predict slightly larger Ce than FRUITY. For instance, for all masses below 4 $M_\odot$ and a metallicity around −0.35 dex, Monash models predict a Ce production 0.32 dex higher than FRUITY. This is caused by a larger number of predicted TP in Monash models than in FRUITY, resulting from the different adopted mass-loss relations (Karakas & Lugaro 2016). On the other hand, we also remark that in Fig. 9, for the two largest masses considered

---

[14] Another source of ^{13}C is present in the top layers of the He-intershell because it is produced in the H-burning shell. However, this source has a negligible impact on the s-process production since most of the produced neutrons are captured by the abundant ^{14}N element.

(5 and 6 $M_\odot$), the Ce production predicted by both sets of models is much lower than for less massive AGB stars (at all metallicities). In such massive AGB stars, the ^{22}Ne(α,n)^{25}Mg neutron source indeed starts to be activated as higher temperatures are reached at the base of the convective zone of the AGB. As indicated in Cristallo et al. (2015), the neutron exposure of ^{22}Ne(α,n)^{25}Mg is smaller than that of the ^{13}C(α,n)^{16}O source. Thus, there is a considerable reduction in the second-peak *s*-process element production. A decrease of the TDU efficiency furthermore accentuates this phenomenon. In fact, as the mass of the exhausted H-core is larger, this implies a larger compression of the H-exhausted layers and a thinner and hotter He-intershell. Therefore, a shorter time is needed to reach the ignition condition for activating the 3α reaction, leading to a shorter interpulse episode and hence a less efficient TDU (Straniero et al. 2003; Cristallo et al. 2015). However, it is interesting to note that almost no Ce is produced in the higher-mass AGB stars of Monash models, whereas FRUITY models predict slightly higher abundances, by about 0.15 dex, for AGB stars with initial masses between 5 and 6 $M_\odot$. This is due to the fact that no ^{13}C pocket is included in the Monash models for such high masses, whereas it is included for smaller masses. Hence, the source of neutrons in these models is only ^{22}Ne(α,n)^{25}Mg, which preferentially creates first-peak *s*-process elements. Such a reaction is also more efficient in the latest TP (while the ^{13}C(α,n)^{16}O reaction is more active in the first TPs; see Karakas & Lugaro 2016). All of this explains the absence of Ce production in Monash models for such high masses.

Regarding the dependency of the Ce production on metallicity, we remark that AGB stars with the lowest metallicity in the FRUITY models considered in this work ($Z = 0.002$, corresponding to [Fe/H] = −0.85 dex) enrich the atmosphere up to [Ce/Fe] < 0.30 dex (before the atmosphere becomes C-rich) only, except for the masses between 3 and 4 $M_\odot$, which [Ce/Fe] reach 0.50 dex. At such low metallicities ([Fe/H] < −0.80 dex), there are indeed fewer heavy seed nuclei available for captured neutrons, which limits the production of heavy elements such as cerium. We note that for even lower metallicities, the production of Ce and Nd is predicted to be larger since the number of available neutrons per seed nuclei (Fe) also becomes larger. Such conditions also favour the production of Pb and Bi.

4.4. Comparing observed and model cerium abundances

In this section, we discuss our comparison of the Ce abundances derived for the Ce AGB sample with the theoretical predictions of FRUITY and Monash models of 5 and 6, 2.50 and 1.50 $M_\odot$ in light of the previous subsections describing both models. We recall that similar results can be found using the Nd AGB sample.

We began this comparison with the stars that have the two highest masses. As already illustrated and discussed in Fig. 9, the most massive AGB stars in each model do not produce [Ce/Fe] abundance ratios larger than ~0.3 dex. Therefore, the larger observed abundances have to be explained by invoking lower stellar masses. This independently confirms the probable absence of massive AGB stars in our sample, as already indicated by the *Gaia*-2MASS diagram shown in Fig. 4.

We then focused on the AGB stars with an initial mass of 2.50 $M_\odot$, since similar conclusions can be obtained for stars of initial mass between 2 and 4 $M_\odot$. Figure 10 shows the [Ce/Fe] ratio predicted after each TDU for the FRUITY and Monash models colour-coded by the C/O abundance ratio. We remark that almost no Ce AGB sample stars are found where models predict the formation of carbon-rich stars, which is in full agreement with our conclusions about the oxygen-rich nature of our sample stars. It can also be seen that the [Ce/Fe] ratio predicted by both models are fully compatible with the observed values. Therefore, for metallicities between −0.80 and 0.00 dex, the yields predicted for AGB stars with an initial mass of 2.50 $M_\odot$ by both models are fully compatible with the observed GSP-Spec Ce abundances that are found between 0.00 and 0.80 dex.

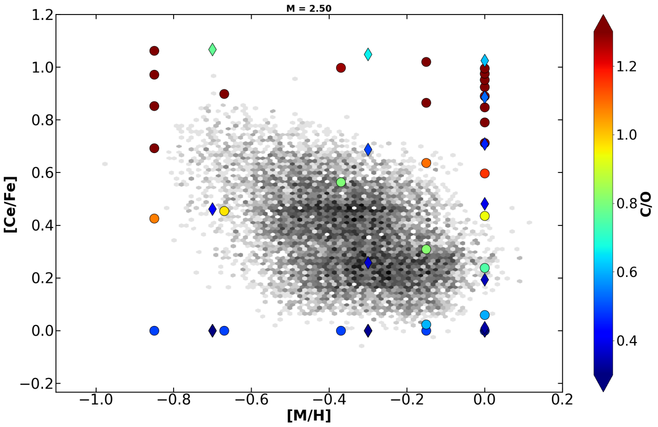

Fig. 10. Cerium AGB sample colour-coded by stellar counts. Filled diamonds (Monash models) and circles (FRUITY ones) correspond to the [Ce/Fe] predicted after each TDU, colour-coded by the C/O ratio. The AGB mass considered here is 2.50 $M_\odot$.

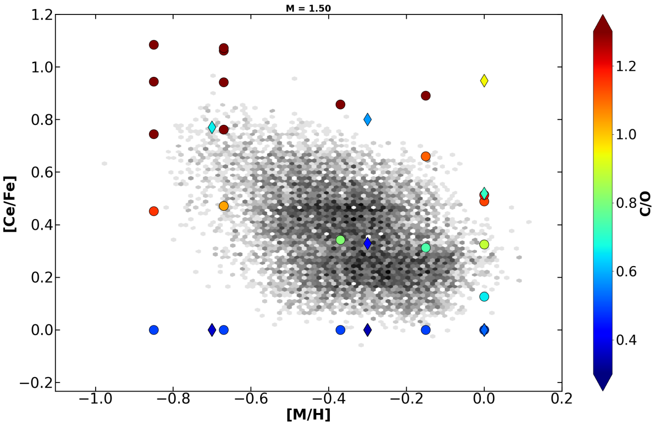

Fig. 11. Same as Fig. 10 but for a mass of 1.50 $M_\odot$.

Figure 11 is similar to Fig. 10 but is for a mass of 1.50 $M_\odot$. For metallicities between −0.40 and −0.10 dex, none of the stars of the Ce AGB sample are located where the models predict that the AGB star atmosphere is C-rich. However, for metallicities around −0.70 dex, we remark that the Monash models predict that the AGB stars are still O-rich, whereas the FRUITY models predict a C-rich atmosphere. As our stars are not C-rich, it seems that the FRUITY models predict a too-large C abundance at the surface of the AGB stars of this mass and metallicity. A similar conclusion can be drawn by looking at stars around solar metallicity. However, we note that we did not detect any stars with a Ce abundance between 0.60 and 0.80 dex at solar metallicity, whereas the Monash models predict such high values for O-rich AGB stars. This could be explained by (i) either the difficulty of automatically detecting the Ce line in RVS crowded spectra of cool metal-rich stars and/or (ii) some Ce overproduction predicted by Monash that is not confirmed by FRUITY. Moreover, the spread of our [Ce/Fe] versus [M/H] can be explained because the AGB stars of our sample have experienced a different number of TDUs. They may also have a large variety of masses and different values of [α/Fe] for a given metallicity. This is also due to the intrinsic dispersion in the formation of the ^{13}C pocket (different profile and masses), even for stars of similar mass and metallicity. Finally, such a spread could also be partially explained by some stars that may be Ba-stars or CH-stars, as mentioned in Sect. 2.1, and thus, the Ce and Nd dispersions could be the result of the dilution effect of the accreted material in the secondary star.

However, heavy *s*-process elements such as Ce and Nd abundances alone are not enough to disentangle this large variety of stellar parameters. For instance, AGB stars of lower metallicities ([Fe/H] < -1 dex) and masses (less than $\sim 3\,M_\odot$) produce large amounts of Pb ([Pb/Fe] > 2 dex; Lugaro et al. 2012; Straniero et al. 2014; Fishlock et al. 2014; Cristallo et al. 2015). Other constraints could also be obtained by looking at light *s*-elements, such as Sr, Y, and Zr. For instance, the [Ce/Y] ratio should decrease with increasing [Fe/H] due to the neutron exposure in the ^{13}C pocket being proportional to the ^{13}C/^{56}Fe ratio. The number of iron seeds is scaled to the metallicity, whereas the ^{13}C is not because of its primary origin (Busso et al. 2001). On the other hand, the production of light *s*-elements should increase with increasing mass because of the activation of the ^{22}Ne(α,n)^{25}Mg neutron source. Indications of the main neutron source (hence the mass) could also be obtained by looking at the [Rb/Zr] ratio (Abia et al. 2001; Karakas & Lugaro 2016; Shejeelammal et al. 2020; Roriz et al. 2021). If this ratio is negative, the main source is ^{13}C(α,n)^{16}O, which provides a relatively low neutron density. As already discussed above, this source is mainly active in low-mass AGB stars. In contrast, a positive [Rb/Zr] ratio is caused by the ^{22}Ne(α,n)^{25}Mg, which produces a higher neutron density that opens branching points and produces Rb. Therefore, further analysis of the complementary *s*-process element abundances in this *s*-process AGB sample may be useful to better understanding and constraining the nucleosynthesis and atmospheric enrichment predicted by AGB models.

5. Summary

We studied the production of *s*-process elements in AGB stars parameterised by the GSP-Spec module from their *Gaia*/RVS spectra. We first confirmed the AGB nature of these stars by looking at their absolute magnitude in the *K*-band using the photogeometric *Gaia* distances (Bailer-Jones et al. 2021) and 2MASS photometry as well as their location in a *Gaia*-2MASS diagram. We also confirmed their oxygen-rich nature. We then defined a high-quality sample (*s*-process AGB sample) of 19 544 AGB stars with Ce and/or Nd abundances after applying a specific GSP-Spec flag combination. The Nd abundances were calibrated through the analysis of the Arcturus spectrum, while no calibration was applied for the Ce abundances, following Contursi et al. (2023).

We then investigated the kinematical and dynamical properties of this *s*-process AGB sample and found that the majority of the stars seem to be located in the Galactic disc. They have indeed a rather low total velocity (<80 km s^{-1}) and a $Z_{\rm max}$ lower than 1.0 kpc. We also found one halo star belonging to the M71 globular cluster. Its atmospheric parameters are fully compatible with studies in the literature, but we found a higher Nd abundance than M71 mean *s*-element abundances. This could be explained by the AGB nature of this star, which is enriched in Nd by successive dredge-up events. We also found four stars belonging to the accreted systems Helmi, Sequoia, GES, and Thamnos. The GES star was found to have a higher Nd abundance than those of the other systems. This higher Nd abundance could be linked to a higher mass of the progenitor. Such a correlation between *s*-process abundances and progenitor mass has already been highlighted with Y in Recio-Blanco et al. (2021) and Ce in Contursi et al. (2023).

The chemical properties of our sample revealed that at a given metallicity, the Ce and Nd abundances are higher for cooler stars. This is an expected feature of the AGB stars and shows the progressive enrichment of their atmosphere in *s*-process elements when more TP and mixing events occur. Moreover, among the 19 544 stars of the *s*-process AGB sample, 1713 stars have both high-quality Ce and Nd abundances that are very well correlated. This is expected, as these two elements belong to the same *s*-process peak and hence have a similar nucleosynthetic origin, showing again the high quality of the GSP-Spec abundances.

We presented a comparison between the GSP-Spec *s*-process abundances and predicted AGB star yields through the FRUITY and Monash models. These models allowed us to first confirm the good correlation found observationally between Ce and Nd abundances. We then examined both models and found that AGB stars with an initial mass between ~ 2 and $\sim 4\,M_\odot$ and metallicities between ~ -0.80 and ~ -0.10 dex are the main Ce producers, reaching [Ce/Fe] > 0.70 dex. In such stars and in those of lower mass, the main neutron source is ^{13}C(α,n)^{16}O and preferentially forms second-peak *s*-process elements such as Ce and Nd. However, Monash models predict slightly higher Ce abundances compared to FRUITY ones due to different physical and computational assumptions. On the other hand, the Ce production in more massive AGB stars (~ 5–$6\,M_\odot$) is much lower, as the main neutron source is ^{22}Ne(α,n)^{25}Mg, leading preferentially to the formation of first-peak *s*-process elements.

Subsequently, we compared these models with the Ce abundances of the Ce AGB sample (similar results can be drawn for Nd AGB sample). The oxygen-rich nature of these sample stars is in agreement with model predictions, although for metallicities around -0.70 dex and masses around $1.50\,M_\odot$, FRUITY could predict a too-high surface carbon enrichment. More importantly, the predicted and GSP-Spec Ce abundances are fully compatible for AGB stars that have an initial mass between ~ 1.5 and $\sim 2.5\,M_\odot$ and metallicities between ~ -0.5 and ~ 0.0 dex.

Finally, all these results confirm the excellent quality of the *Gaia* data and the GSP-Spec chemical abundances, leading to a very large sample of AGB stars with second-peak *s*-process element abundances. Future studies may explore the abundances of other chemical species, such as Sr, Y, Zr, Rb, and/or Pb, in order to better constrain the yield predictions.

Acknowledgements. A.R.B. and Pd.L. acknowledge support from the European Union's Horizon 2020 research and innovation program under SPACE-H2020 grant agreement number 101004214 (EXPLORE project). P.A.P. thanks the Centre National d'Études Spatiales (CNES) for funding support. C.A. acknowledges partial support by project PID2021-123110NB-I00 financed by MCIN/AEI/10.13039/501100011033/FEDER, UE. We sincerely thank Sergio Cristallo and Amanda Karakas for fruitful discussion. Special thanks to Niels Nieuwmunster for his grateful comments on some figures. This work has made use of data from the European Space Agency (ESA) mission *Gaia* (`https://www.cosmos.esa.int/gaia`), processed by the *Gaia* Data Processing and Analysis Consortium (DPAC, `https://www.cosmos.esa.int/web/gaia/dpac/consortium`). Funding for the DPAC has been provided by national institutions, in particular the institutions participating in the *Gaia* Multilateral Agreement.

References

Abia, C., Busso, M., Gallino, R., et al. 2001, ApJ, 559, 1117
Abia, C., Domínguez, I., Gallino, R., et al. 2002, ApJ, 579, 817
Abia, C., de Laverny, P., Romero-Gómez, M., & Figueras, F. 2022, A&A, 664, A45
Arlandini, C., Käppeler, F., Wisshak, K., et al. 1999, ApJ, 525, 886
Asplund, M., Grevesse, N., Sauval, A. J., & Scott, P. 2009, ARA&A, 47, 481
Bailer-Jones, C. A. L., Rybizki, J., Fouesneau, M., Demleitner, M., & Andrae, R. 2021, AJ, 161, 147
Baumgardt, H., & Hilker, M. 2018, MNRAS, 478, 1520
Belokurov, V., Erkal, D., Evans, N. W., Koposov, S. E., & Deason, A. J. 2018, MNRAS, 478, 611
Bijaoui, A. 2012, in Seventh Conference on Astronomical Data Analysis, eds. J. L. Starck, & C. Surace, 2
Birch, K. P., & Downs, M. J. 1994, Metrologia, 31, 315
Bisterzo, S., Gallino, R., Straniero, O., Cristallo, S., & Käppeler, F. 2011, MNRAS, 418, 284
Bisterzo, S., Gallino, R., Käppeler, F., et al. 2015, MNRAS, 449, 506
Bisterzo, S., Travaglio, C., Wiescher, M., et al. 2016, J. Phys. Conf. Ser., 665, 012023
Boesgaard, A. M., King, J. R., Cody, A. M., Stephens, A., & Deliyannis, C. P. 2005, ApJ, 629, 832
Busso, M., Gallino, R., & Wasserburg, G. J. 1999, ARA&A, 37, 239
Busso, M., Gallino, R., Lambert, D. L., Travaglio, C., & Smith, V. V. 2001, ApJ, 557, 802
Cameron, A. G. W. 1960, AJ, 65, 485
Carretta, E., Bragaglia, A., Gratton, R., D'Orazi, V., & Lucatello, S. 2009, A&A, 508, 695
Choplin, A., Siess, L., & Goriely, S. 2022, A&A, 667, A155
Contursi, G., de Laverny, P., Recio-Blanco, A., & Palicio, P. A. 2021, A&A, 654, A130
Contursi, G., de Laverny, P., Recio-Blanco, A., et al. 2023, A&A, 670, A106
Cristallo, S., Straniero, O., Gallino, R., et al. 2009, ApJ, 696, 797
Cristallo, S., Piersanti, L., Straniero, O., et al. 2011, ApJS, 197, 17
Cristallo, S., Straniero, O., Piersanti, L., & Gobrecht, D. 2015, ApJS, 219, 40
Cristallo, S., Karinkuzhi, D., Goswami, A., Piersanti, L., & Gobrecht, D. 2016, ApJ, 833, 181
Cseh, B., Világos, B., Roriz, M. P., et al. 2022, A&A, 660, A128
Danziger, I. J. 1966, ApJ, 143, 527
Den Hartog, E. A., Lawler, J. E., Sneden, C., & Cowan, J. J. 2003, ApJS, 148, 543
Fanelli, C., Origlia, L., Oliva, E., et al. 2021, A&A, 645, A19
Feuillet, D. K., Feltzing, S., Sahlholdt, C. L., & Casagrande, L. 2020, MNRAS, 497, 109
Feuillet, D. K., Sahlholdt, C. L., Feltzing, S., & Casagrande, L. 2021, MNRAS, 508, 1489
Fishlock, C. K., Karakas, A. I., Lugaro, M., & Yong, D. 2014, ApJ, 797, 44
Gaia Collaboration (Vallenari, A., et al.) 2023a, A&A, 674, A1
Gaia Collaboration (Recio-Blanco, A., et al.) 2023b, A&A, 674, A38
Gallino, R., Arlandini, C., Busso, M., et al. 1998, ApJ, 497, 388
Gerber, J. M., Friel, E. D., & Vesperini, E. 2020, AJ, 159, 50
Goriely, S., & Siess, L. 2004, A&A, 421, L25
Grevesse, N., Asplund, M., & Sauval, A. J. 2007, Space Sci. Rev., 130, 105
Harris, W. E. 1996, AJ, 112, 1487
Hayes, C. R., Masseron, T., Sobeck, J., et al. 2022, ApJS, 262, 34
Helmi, A. 2020, ARA&A, 58, 205
Helmi, A., Babusiaux, C., Koppelman, H. H., et al. 2018, Nature, 563, 85
Herwig, F. 2004, ApJ, 605, 425
Hinkle, K., Wallace, L., Valenti, J., & Harmer, D. 2000, Visible and Near Infrared Atlas of the Arcturus Spectrum 3727–9300 Å (San Francisco: ASP)
Iben, I., Jr. 1975, ApJ, 196, 549
Iben, I., Jr., & Renzini, A. 1983, ARA&A, 21, 271
Jönsson, H., Holtzman, J. A., Allende Prieto, C., et al. 2020, AJ, 160, 120
Käppeler, F., Gallino, R., Bisterzo, S., & Aoki, W. 2011, Rev. Mod. Phys., 83, 157
Karakas, A. I., & Lattanzio, J. C. 2014, PASA, 31, e030
Karakas, A. I., & Lugaro, M. 2016, ApJ, 825, 26
Karakas, A. I., Lattanzio, J. C., & Pols, O. R. 2002, PASA, 19, 515
Karakas, A. I., Lugaro, M., Carlos, M., et al. 2018, MNRAS, 477, 421
Koppelman, H. H., Helmi, A., Massari, D., Price-Whelan, A. M., & Starkenburg, T. K. 2019, A&A, 631, L9
Lamb, S. A., Howard, W. M., Truran, J. W., & Iben, I., Jr. 1977, ApJ, 217, 213
Lambert, D. L. 1991, in Evolution of Stars: The Photospheric Abundance Connection, eds. G. Michaud, & A. V. Tutukov, 145, 299
Lambert, D. L., Smith, V. V., Busso, M., Gallino, R., & Straniero, O. 1995, ApJ, 450, 302
Lebzelter, T., Mowlavi, N., Marigo, P., et al. 2018, A&A, 616, L13
Lebzelter, T., Mowlavi, N., Lecoeur-Taibi, I., et al. 2023, A&A, 674, A15
Limongi, M., & Chieffi, A. 2018, ApJS, 237, 13
Lodders, K. 2003, ApJ, 591, 1220
Lugaro, M., Karakas, A. I., Stancliffe, R. J., & Rijs, C. 2012, ApJ, 747, 2
Lugaro, M., Campbell, S. W., D'Orazi, V., et al. 2016, J. Phys. Conf. Ser., 665, 012021
Marigo, P. 2002, A&A, 387, 507
Masseron, T., García-Hernández, D. A., Mészáros, S., et al. 2019, A&A, 622, A191
Matsuno, T., Koppelman, H. H., Helmi, A., et al. 2022, A&A, 661, A103
Messineo, M. 2023, A&A, 671, A148
Myeong, G. C., Evans, N. W., Belokurov, V., Amorisco, N. C., & Koposov, S. E. 2018, MNRAS, 475, 1537
Myeong, G. C., Vasiliev, E., Iorio, G., Evans, N. W., & Belokurov, V. 2019, MNRAS, 488, 1235
Palicio, P. A., Recio-Blanco, A., Poggio, E., et al. 2023, A&A, 670, L7
Peters, J. G. 1968, ApJ, 154, 225
Pignatari, M., Gallino, R., Heil, M., et al. 2010, ApJ, 710, 1557
Prantzos, N., Abia, C., Limongi, M., Chieffi, A., & Cristallo, S. 2018, MNRAS, 476, 3432
Prantzos, N., Abia, C., Cristallo, S., Limongi, M., & Chieffi, A. 2020, MNRAS, 491, 1832
Ramírez, S. V., & Cohen, J. G. 2002, AJ, 123, 3277
Recio-Blanco, A., de Laverny, P., Allende Prieto, C., et al. 2016, A&A, 585, A93
Recio-Blanco, A., Fernández-Alvar, E., de Laverny, P., et al. 2021, A&A, 648, A108
Recio-Blanco, A., de Laverny, P., Palicio, P. A., et al. 2023, A&A, 674, A29
Roriz, M. P., Lugaro, M., Pereira, C. B., et al. 2021, MNRAS, 501, 5834
Rybizki, J., Green, G. M., Rix, H.-W., et al. 2022, MNRAS, 510, 2597
Sanders, J. L., & Matsunaga, N. 2023, MNRAS, 521, 2745
Shejeelammal, J., Goswami, A., Goswami, P. P., Rathour, R. S., & Masseron, T. 2020, MNRAS, 492, 3708
Skrutskie, M. F., Cutri, R. M., Stiening, R., et al. 2006, AJ, 131, 1163
Smith, V. V., & Lambert, D. L. 1985, ApJ, 294, 326
Smith, V. V., & Lambert, D. L. 1986, ApJ, 311, 843
Smith, V. V., & Lambert, D. L. 1988, ApJ, 333, 219
Smith, V. V., Lambert, D. L., & McWilliam, A. 1987, ApJ, 320, 862
Sneden, C., Kraft, R. P., Langer, G. E., Prosser, C. F., & Shetrone, M. D. 1994, AJ, 107, 1773
Soszyński, I., Gieren, W., & Pietrzyński, G. 2005, PASP, 117, 823
Straniero, O., Gallino, R., Busso, M., et al. 1995, ApJ, 440, L85
Straniero, O., Domínguez, I., Cristallo, S., & Gallino, R. 2003, PASA, 20, 389
Straniero, O., Cristallo, S., & Piersanti, L. 2014, ApJ, 785, 77
Straniero, O., Abia, C., & Domínguez, I. 2023, Eur. Phys. J. A, 59, 17
Tautvaišienė, G., Viscasillas Vázquez, C., Mikolaitis, Š., et al. 2021, A&A, 649, A126
Ulrich, R. K. 1973, in Explosive Nucleosynthesis, eds. D. N. Schramm, & W. D. Arnett, 139
Utsumi, K. 1970, PASJ, 22, 93
Vanture, A. D. 1992, AJ, 104, 1997

Appendix A: ADQL query

```
SELECT source_id
FROM gaiadr3.astrophysical_parameters inner join
gaiadr3.gaia_source using(source_id)
WHERE
(rv_expected_sig_to_noise>0)
AND
(vbroad<=13)
AND
(teff_gspspec IS NOT NULL)
AND
(teff_gspspec<=4000)
AND
(ndfe_gspspec IS NOT NULL)
AND
( (ndfe_gspspec_upper-ndfe_gspspec_lower)<=0.40)
AND
(flags_gspspec LIKE '0%')
AND
(flags_gspspec LIKE '_0%')
AND
(flags_gspspec LIKE '__0%')
AND
(flags_gspspec LIKE '___0%')
AND
(flags_gspspec LIKE '____0%')
AND
(flags_gspspec LIKE '_____0%')
AND
(flags_gspspec LIKE '______0%')
AND
((flags_gspspec LIKE '_______0%') OR (flags_gspspec
LIKE '_______1%') )
AND
(flags_gspspec LIKE '________0%')
AND
(flags_gspspec LIKE '_________0%')
AND
(flags_gspspec LIKE '__________0%')
AND
(flags_gspspec LIKE '___________0%')
AND
(flags_gspspec LIKE '____________0%')
AND
((flags_gspspec LIKE '%0___') OR (flags_gspspec
LIKE '%1___') OR (flags_gspspec LIKE '%2___'))
AND
((flags_gspspec LIKE '%0__') OR (flags_gspspec LIKE
'%1__') )
AND
NOT
((ndfe_gspspec>1.99) AND (flags_gspspec LIKE
    '____________0%') AND (flags_gspspec NOT LIKE
    '%0___'))
```

Listing 1. `ADQL` query for the *Nd AGB sample*. We note that this query returns non-calibrated log(g).